Autonomous Ultrasound-Guided Tissue Dissection

Philip Pratt[1], Archie Hughes-Hallett[2], Lin Zhang[1], Nisha Patel[1,2]
Erik Mayer[2], Ara Darzi[1,2], and Guang-Zhong Yang[1]

[1] Hamlyn Centre for Robotic Surgery,
Imperial College of Science, Technology and Medicine,
London SW7 2AZ, UK
[2] Department of Surgery and Cancer,
Imperial College of Science, Technology and Medicine,
London SW7 2AZ, UK
{p.pratt,a.hughes-hallett,lin.zhang11,nisha.patel2,
e.mayer,a.darzi,g.z.yang}@imperial.ac.uk

Abstract. Intraoperative ultrasound imaging can act as a valuable guide during minimally invasive tumour resection. However, contemporaneous bimanual manipulation of the transducer and cutting instrument presents significant challenges for the surgeon. Both cannot occupy the same physical location, and so a carefully coordinated relative motion is required. Using robotic partial nephrectomy as an index procedure, and employing PVA cryogel tissue phantoms in a reduced dimensionality setting, this study sets out to achieve autonomous tissue dissection with a high velocity waterjet under ultrasound guidance. The open-source da Vinci Research Kit (DVRK) provides the foundation for a novel multimodal visual servoing approach, based on the simultaneous processing and analysis of endoscopic and ultrasound images. Following an accurate and robust Jacobian estimation procedure, dissections are performed with specified theoretical tumour margin distances. The resulting margins, with a mean difference of 0.77mm, indicate that the overall system performs accurately, and that future generalisation to 3D tumour and organ surface morphologies is warranted.

1 Introduction

Many contemporary minimally invasive surgical procedures stand to benefit from intraoperative ultrasound guidance as a means of overcoming the haptic deficit imposed by having restricted access. In the context of cancerous tumour resection, the modality can provide excellent views of the interface between healthy and diseased tissues. One such case is robotic partial nephrectomy, adopted by this study as a clinical exemplar, through which the nephron-sparing approach offers the best long-term patient prognoses. However, experience tells us that the ideal paradigm of simultaneous guidance and dissection is very difficult to achieve in practice, even when registration [1] is used to co-locate endoscopic and ultrasound images. Nonetheless, rapid progress in the field of autonomous robotic surgical systems [2] points toward novel solutions to this problem. It can only be a matter of time before tumour resection requires the surgeon only in a supervisory role.

N. Navab et al. (Eds.): MICCAI 2015, Part I, LNCS 9349, pp. 249–257, 2015.
DOI: 10.1007/978-3-319-24553-9_31

Notable examples of such systems include the Probot [3], an early computer-controlled robot capable of performing transurethral resection of the prostate (TURP), successfully translated through to human clinical trials. Preoperative transrectal ultrasound, combined with a curve-fitting procedure, was used to build 3D models of the target resection volume. Recently, the open-source da Vinci Research Kit (DVRK) [4] has facilitated a 'robotic ultrasound surgical assistant' [5], whereby the imaging plane of a 'pick-up' transducer automatically follows the tips of other instruments engaged in resection tasks. These distal coordinate frames are related to each other through an initial registration of the robot arm base frames. The current proliferation of research kits promises to accelerate progress in these areas.

The use of waterjet dissection in nephron-sparing renal surgery [6] can reduce morbidity associated with intraoperative haemorrhage. The selective action of the waterjet, leading to preservation of arterial tissue, makes off-clamp dissection with precise haemostasis possible. While the use of robotic waterjet systems has seen applications in engineering [7], to date no precedents have been set in the surgical domain. Building on these separate approaches, this study aims to establish the trifecta of autonomous robotic control, guidance through ultrasound imaging and waterjet tumour resection. In comparison to the complex scissor-like action of traditional cutting tools, the linearity of the jet greatly simplifies instrument manipulation. To achieve sufficient accuracy, visual servoing is employed but with, for the first time, input from multiple imaging sources. Working in a reduced dimensionality (2D) setting ensures that the problem is tractable at the outset.

2 Materials and Methods

2.1 Experimental Setup

Having a tensile strength and elasticity similar to human renal parenchyma, bespoke polyvinyl alcohol (PVA) phantoms [8] were used to simulate 2D tumour boundaries. A shallow rectangular tray was filled to a depth of 5mm with 10% PVA solution (by weight), to which cellulose powder (2% by weight) had been added to improve echogenic contrast, and subjected to an initial freeze/thaw cycle. Curved paths were cut in this layer (figure 1, left), and the sections separated in order to make two separate phantoms. Each tray was then filled to a total depth of 10mm with cellulose-free cryogel and subjected to a final freeze/thaw cycle. The resulting phantoms represent completely endophytic lesions with boundaries invisible from the surface.

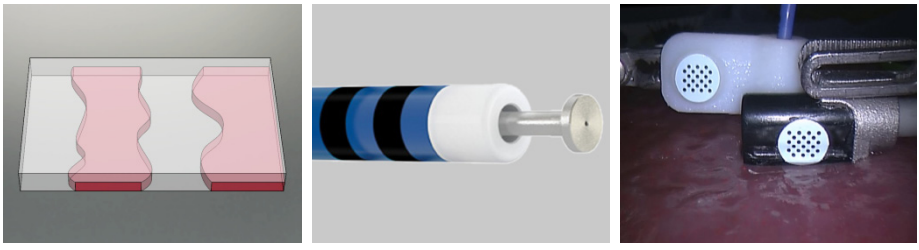

Fig. 1. Cryogel phantom (left); waterjet 'T-type' nozzle (middle); pattern mountings (right)

A 'T-type' HybridKnife (ERBE Elektromedizin, GmbH, Tuebingen, Germany), was connected to an ERBEJET2 double-piston pump cartridge and giving set with fluid bag containing 0.9% saline. The waterjet nozzle (figure 1, middle) has a diameter of 120µm, and the pump was configured with the maximum pressure setting of 80 bar. A custom mounting was 3D-printed in hard plastic material (figure 1, right), providing a platform for a KeyDot® tracking marker (KeySurgical Inc., Eden Prairie, MN, USA), and a foot allowing the nozzle to be grasped by robotic Cadiere forceps. Details regarding the ultrasound transducer, metal mounting bracket, calibration procedure, and KeyDot tracking algorithms are described in previous work [9]. To facilitate instrument identification, the two patterns were arranged in opposition.

2.2 System Architecture

The overall system architecture is illustrated in figure 2. An intact 'standard' da Vinci Surgical System (Intuitive Surgical, Sunnyvale, CA, USA) was connected to the DVRK [4], capable of controlling two patient side manipulators (PSMs). This in turn was connected to a Linux server, running various *cisst*/SAW/ROS components [4], over an IEEE-1394 Firewire link. Video feeds from the (stereo) endoscope and ultrasound cart were captured on a separate Windows machine using the Quadro digital video pipeline (Nvidia Corporation, Santa Clara, CA, USA). The tracking, visual servoing control and dissection software runs on the latter machine. Kinematic states were updated and queried continuously over a lightweight UDP network interface. The ERBEJET2 foot pedal cannot be replaced by a computer-controlled relay, and was therefore operated manually in response to visual cues from the control machine. In this study, the endoscopic camera manipulator (ECM) remains in a fixed position during dissection. The intrinsic properties and distortion coefficients of the camera were calibrated using the benchmark OpenCV implementation [10].

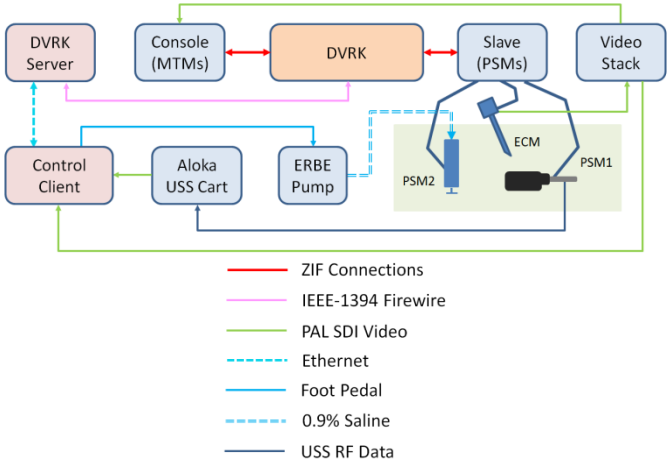

Fig. 2. Schematic diagram illustrating system architecture

2.3 Robust Jacobian Estimation

In the reduced dimensionality setting, where only end effector translations are considered, the 3-DOF Jacobian estimation is equivalent to finding the rotation matrix relating the camera and robot arm base coordinate systems. Generalisation must wait until the salient features of the overall approach are proven. Unfortunately, a simple two-sided finite difference approximation to the Jacobian matrix entries, generated by issuing orthogonal movements along the Cartesian axes in the PSM base frames B_i, was found to be very unreliable and subject to the hysteretic behaviour of the robot and its low-level control system.

Instead, 10 incremental movements were issued along each of the positive and negative X, Y and Z axes of the PSM base frame, respectively (5 outward and 5 inward), resulting in a total of 60 pose increments in the camera frame from which the Jacobian entries were estimated. For each entry, the median value was chosen in order to remove outlier motions, and then the whole matrix was subjected to the Gram-Schmidt orthogonalisation process. At the start of each dissection experiment, the end effectors were carefully teleoperated into parallel orientations orthogonal to the phantom surface. The PSM1 and PSM2 Jacobians $J_{1,2}$ were then estimated sequentially. The visual servoing loops were implemented as simple proportional controllers embedded in a finite state machine (FSM), where error signals $d\tilde{p}_i$ in the camera frames generated incremental movements $d\tilde{e}_i$ in the Cartesian robot frames, until the targets were reached within a tolerance of 0.4mm. Together with an empirically chosen gain coefficient of 0.04, an appropriate rate was set for the cutting action of the waterjet.

2.4 Coordinate Frame Relationships

Figure 3 illustrates the physical components required to perform the dissection task, their respective coordinate systems, and the relationships between incremental movements in the PSM and camera frames. The notation $T^{S\to D}$ is used to represent the transformation (constant, or otherwise) from a source coordinate frame S to the destination frame D. In addition, several constant geometric quantities were specified, either as free parameters, through measurement, or via calibration, as follows: a) the ultrasound image to probe pattern transformation $T^{U\to P_1}$ and pixel-to-millimetre scale

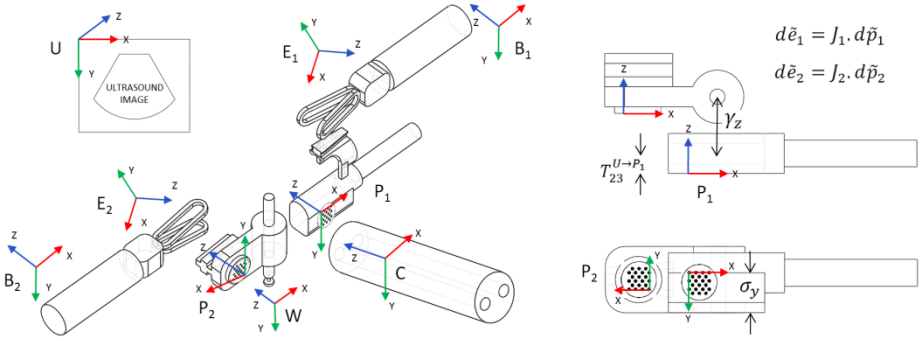

Fig. 3. Exploded view of system components and associated coordinate frames

factor s (calibrated); b) the waterjet tip to PSM2 pattern transformation $T^{W \to P_2}$ (known from the mount CAD model); c) the theoretical (i.e. intended) dissection margin μ_x; d) the Y displacement σ_y from the PSM1 pattern origin to the bottom surface of the ultrasound transducer casing; and e) the Z displacement γ_z in the probe pattern frame from the transducer to the waterjet tip.

2.5 Visual Servoing with Multimodal Inputs

Each dissection run comprises four stages: initialisation, instrument alignment, dissection path generation and waterjet engagement. During initialisation, the transducer is teleoperated (translation only) into a position crossing the tumour boundary, making contact with the phantom surface. The current state of the PSM end effectors $T^{E_1 \to B_1}$ and $T^{E_2 \to B_2}$ is queried from the DVRK. Furthermore, the target ultrasound abscissa α^{target} is stored. In subsequent movements of the probe, the visual servoing loop seeks to keep the abscissa constant. Figure 4 (left) illustrates how the region of interest is chosen (bounded by green lines), and the subsequent median filtered [10] and thresholded images. The location of the abscissa is estimated in the latter by taking the mean of the pixel X coordinates where, for each scan line left to right, the image first crosses into a non-zero intensity (yellow line).

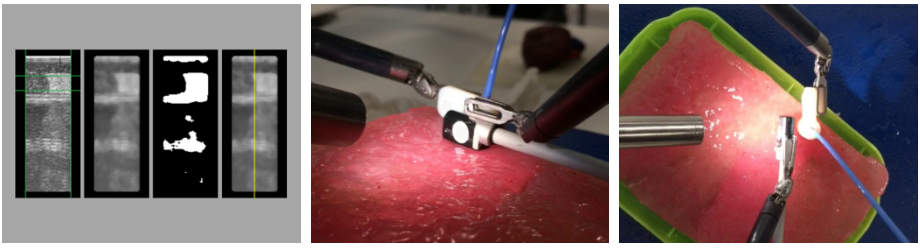

Fig. 4. Ultrasound image processing (left); side/aerial views of dissection (middle/right)

The next stage begins with teleoperation of PSM2 into an approximately correct initial position behind the transducer. Equation 1 gives the adjustment to PSM2 in the camera frame C required to bring the waterjet into alignment with the tumour boundary, taking into account the specified margin. It amounts to the difference between the desired and current positions of the waterjet tip. This vector is passed to the servoing FSM in order to move PSM2 into the required initial position.

$$T^{P_1 \to C}.\left[s.\alpha^{target} + T_{03}^{U \to P_1} - \mu_x,\ \sigma_y,\ T_{23}^{U \to P_1} + \gamma_z\right]^{\top} - T^{P_2 \to C}.T^{W \to P_2}.[0,0,0]^{\top} \quad (1)$$

2.6 Dissection Path Generation

Equation 2 describes the PSM1 adjustments in the camera frame C required to advance the probe continuously by a distance Δz in the pattern frame P_1 while accounting for movement in the ultrasound abscissa relative to the target value ($\Delta z = -1\text{mm}$ in all experiments). With reference to figure 5, PSM1 reactively follows the boundary path

$[x_i, y_i, z_i]^\top$ in the static camera coordinate frame C, but the intention is that PSM2 proactively follows the measured position of the boundary $[u_i, v_i, w_i]^\top$, while also accounting for the theoretical margin. To achieve this, the latter waterjet tip pathway is stored in the static camera frame C, leading to the sequence of PSM2 adjustments embodied in equation 3. When the tip Z position lies outside of the stored pathway, the first entry is adopted. The signal to engage the waterjet is given only when the tip reaches the start of the pathway. The spatial displacement γ_z between transducer and jet leads to a small, but inevitable delay before engagement.

$$T_i^{P_1 \to C}.[s.(\alpha_i - \alpha^{target}),\ 0,\ \Delta z]^\top - T_i^{P_1 \to C}.[0,0,0]^\top \tag{2}$$

$$[u_i, v_i, w_i]^\top - T_i^{P_2 \to C}.T^{W \to P_2}.[0,0,0]^\top \tag{3}$$

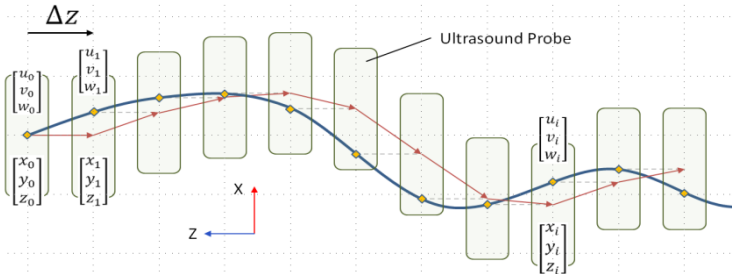

Fig. 5. Plan view: tumour boundary (blue) and its relationship to the PSM1 trajectory (red)

3 Results

3.1 Jacobian Estimation

In order to test the repeatability of the proposed multi-step 3-DOF Jacobian estimation procedure, eight runs for PSM1 were performed. For one such run, figure 6 illustrates the characteristics of the Y component of the pose changes made in response to the X/Y/Z sequence of orthogonal 1.0mm end effector increments. Median values appear as dashed lines. It is clear from this and from the observation of other runs that certain incremental motions result in significant outliers which, if ignored, render any Jacobian estimate unreliable, to the detriment of the visual servoing loop. This phenomenon explains the very poor behaviour of naïve two-sided approximations. The current DVRK control implementation does not compensate for the effects of gravity, and this is most evident in the Y pose change component (the endoscope having an upright orientation). In contrast, following analysis of the repeated multi-step runs, the largest standard deviation of each of the resulting Jacobian matrix entries is 0.01mm. The maximum range of any entry is 0.04mm, and pairwise comparison with the first run leads to a maximum Frobenius norm of 0.058. The procedure is therefore seen to be highly repeatable and capable of overcoming hardware inaccuracies.

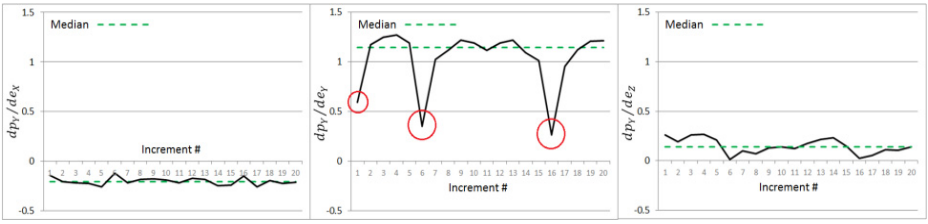

Fig. 6. The Y component of pose changes showing median values (outliers highlighted in red)

3.2 Tissue Dissection

Eight dissection experiments were performed using two theoretical margin settings and a pair of cryogel tissue phantoms. Figure 7 (left) illustrates the delayed relative motion of the ultrasound probe and waterjet during a typical run. A sequence of four video snapshots is shown, stacked top-to-bottom, and with reference to figure 5, it can be seen that the X components of the trajectories in the camera frame follow related, but temporally displaced paths. Example dissections are circled in figure 7 (middle). The fissure lengths range from 6.3mm to 14.7mm, with a mean length of 8.3mm. At present, limitations of the DVRK ECM power supply do not permit automatic control of the camera position, and thus the maximum dissection length is bounded above. Figure 7 (right) illustrates post-dissection margin measurement. A series of circle centres is identified on the fissure edge proximal to the resection target. Subsequently, the circle radii are adjusted so that they just touch the material interface. The reference measure with 1mm gradations appears on the right.

Fig. 7. Delayed relative motion of ultrasound probe and waterjet (left); phantom reverse showing dissection paths (middle); margin measurement (right)

Figure 8 show the specified theoretical margins (initial two runs at 3mm, the remainder at 3.75mm), and the measured margins with standard deviations. It also shows the margin ranges for each run, defined as the difference between maximum and minimum margin measurements. All such ranges are sub-millimetre, meaning that the deviation in the amount of 'healthy tissue' left behind is very small. Over all experiments, the mean difference between theoretical and measured margins is 0.77mm. Putting this into context, the widths of the fissures left by the waterjet were found to range up to 1.35mm (i.e. the maximum hole radius was approximately 0.67mm). This is due to the finite extent of the jet itself, and vibration induced by the high-velocity flow. It can be seen from the measured margin and ranges, and indeed visual inspection, that no 'positive' margins were present following any of the experiments.

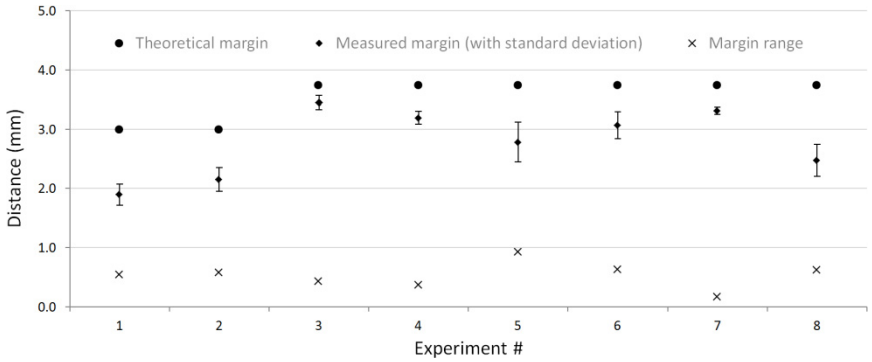

Fig. 8. Comparison of theoretical and measured margins (including ranges)

These results indicate that the cutting is sufficiently consistent and accurate, but also highlight the fact that the extent of the waterjet fissure must be calibrated for each tissue/material type, in accordance with the waterjet pressure setting, if the specified margin distance is to be met in practice.

4 Conclusion

This preliminary study sets an important precedent for the future of autonomous robotic surgical systems. Only through vision-based control can such systems ever hope to match the performance of human operators in the dynamic and variegated context of demanding surgical tasks. The machine approach has one crucial advantage over human counterparts, in that control systems can be designed to process multiple visual sources, with complementary modalities, in a contemporaneous and proportionate manner. The foundation herein evidently leads to a cumulative programme of generalisation, starting in the 2D realm but adopting dissection targets with circular topologies. Ultimately, this will lead to spherical topologies in 3D with patient-specific organ surface shapes, where real time dense stereo surface reconstruction and freehand 3D volume reconstruction will come into play. Robust methods for active 6-DOF Jacobian estimation and will be required, in addition to effector tracking algorithms reliable in the presence of occlusions. Finally, the waterjet delivery mechanism must adopt curvilinear profiles, capable of enucleation while avoiding iatrogenic injury, thereby simultaneously optimising the outcomes of cancer surgery.

References

1. Hughes-Hallett, A., Pratt, P., Mayer, E., Di Marco, A., Yang, G.-Z., Vale, J., Darzi, A.: Intraoperative ultrasound overlay in robot-assisted partial nephrectomy: first clinical experience. European Urology 65(3), 671–672 (2014)
2. Moustris, G., Hiridis, S., Deliparaschos, K., Konstantinidis, K.: Evolution of autonomous and semi-autonomous robotic surgical systems: a review of the literature. International Journal of Medical Robotics and Computer Assisted Surgery 7(4), 375–392 (2011)

3. Harris, S., Arambula-Cosio, F., Mei, Q., Hibberd, R.D., Davies, B., Wickham, J., Nathan, M., Kundu, B.: The Probot – an active robot for prostate resection. Proceedings of the Institution of Mechanical Engineers 211(H), 317–325 (1997)
4. Kazanzides, P., Chen, Z., Deguet, A., Fischer, G., Taylor, R., DiMaio, S.: An open-source research kit for the da Vinci surgical system. In: Proceedings of the IEEE International Conference on Robotics and Automation, pp. 6434–6439 (2014)
5. Mohareri, O., Salcudean, S.: da Vinci® auxiliary arm as a robotic surgical assistant for semi-autonomous ultrasound guidance during robot-assisted laparoscopic surgery. In: Proceedings of the 7th Hamlyn Symposium on Medical Robotics, pp. 45–46 (2014)
6. Basting, R., Djakovic, N., Widmann, P.: Use of water jet resection in organ-sparing kidney surgery. Journal of Endourology 14(6), 501–505 (2000)
7. Davis, D.: Robotic abrasive water jet cutting of aerostructure components. Automated Waterjet Cutting Processes, Society of Manufacturing Engineers, Detroit Michigan (1988)
8. Surry, K., Austin, J., Fenster, A., Peters, T.: Poly(vinyl alchohol) cryogel phantoms for use in ultrasound and MR imaging. Physics in Medicine and Biology 49(24), 5529–5546 (2004)
9. Pratt, P., Jaeger, A., Hughes-Hallett, A., Mayer, E., Vale, J., Darzi, A., Peters, T., Yang, G.-Z.: Robust ultrasound probe tracking: initial clinical experiences during robot-assisted partial nephrectomy. Information Processing and Computer-Assisted Interventions (2015)
10. Bradski, G., Kaehler, A.: Learning OpenCV: Computer vision with the OpenCV library. O'Reilly Media, Inc. (2008)